Environmental Science
Processes & Impacts

Glass Surface Evolution Following Gas Adsorption and Particle Deposition from Indoor Cooking Events as Probed by Microspectroscopic Imaging and Characterization

Journal:	*Environmental Science: Processes & Impacts*
Manuscript ID	EM-ART-04-2020-000156.R1
Article Type:	Paper

Environmental Significance Statement

Chemical reactions on indoor surfaces play an important role in air quality in indoor environments, where humans spend 90% of their time. Direct measurements of the physical and chemical state of these surfaces provide insights into the underlying physical and chemical processes involving surface adsorption, surface partitioning and particle deposition. Window glass, a ubiquitous indoor surface, placed vertically during indoor cooking activities in the House Observations of Microbial and Environmental Chemistry (HOMEChem) campaign was analyzed using microspectropic probes. These surfaces are shown to be important sinks for organic rich particles and particle deposition contributes enough organic matter from a single day of exposure equivalent to a uniform film two nanometers thick. Chemically distinct changes are observed for different cooking activities.

Glass Surface Evolution Following Gas Adsorption and Particle Deposition from Indoor Cooking Events as Probed by Microspectroscopic Analysis

Authors : Victor W. Or[1], Michael Wade[2], Sameer Patel[3], Michael R. Alves[1], Deborah Kim[1], Sarah Schwab[1], Hannah Przelomski[4], Rachel O'Brien[4], Donghyun Rim[5], Richard L. Corsi[6], Marina E. Vance[3], Delphine K. Farmer[7], and Vicki H. Grassian[1,8]

Affiliations:

[1] Department of Chemistry and Biochemistry, University of California San Diego, La Jolla, California 92093, USA

[2] Department of Civil, Architectural and Environmental Engineering, Cockrell School of Engineering, The University of Texas at Austin, Austin, Texas 78712, USA

[3] Mechanical Engineering Department, University of Colorado Boulder, Boulder, Colorado 80309, USA

[4] Department of Chemistry, William & Mary, Williamsburg, Virginia 23185, USA

[5] Department of Architectural Engineering, Pennsylvania State University, University Park, Pennsylvania 16802, USA

[6] Maseeh College of Engineering & Computer Science, Portland State University, Portland, Oregon 97021, USA

[7] Department of Chemistry, Colorado State University, Fort Collins, Colorado 80523, USA

[8] Scripps Institution of Oceanography and Department of Nanoengineering, University of California, San Diego, La Jolla, California 92093, USA

Abstract

Indoor surfaces are extremely diverse and their interactions with airborne compounds and aerosols influence the lifetime and reactivity of indoor emissions. Direct measurements of the physical and chemical state of these surfaces provide insights into the underlying physical and chemical processes involving surface adsorption, surface partitioning and particle deposition. Window glass, a ubiquitous indoor surface, was placed vertically during indoor activities throughout the House Observations of Microbial and Environmental Chemistry (HOMEChem) campaign and then analyzed to measure changes in surface morphology and surface composition. Atomic force microscopy-infrared (AFM-IR) spectroscopic analyses reveal that deposition of submicron particles from cooking events is a contributor to modifying the chemical and physical state of glass surfaces. These results demonstrate that the deposition of glass surfaces can be an important sink for organic rich particles material indoors. These findings also show that particle deposition contributes enough organic matter from a single day of exposure equivalent to a uniform film up to two nanometers in thickness, and that the chemical distinctness of different indoor activities is reflective of the chemical and morphological changes seen in these indoor surfaces. Comparison of the experimental results to physical deposition models shows variable agreement, suggesting that processes not captured in physical deposition models may play a role in the sticking of particles on indoor surfaces.

Introduction

Humans spend a majority of their time indoors[1] and there has been an emerging interest in studying the fundamental chemistry influencing the quality of indoor air to which occupants are exposed.[2,3] Increased effort in indoor chemistry research has been directed towards the characterization and chemistry of gases and aerosols in indoor air.[2,4–8] Surfaces and their influence on indoor air quality have begun to receive more attention, as surfaces are important not only for gas-phase adsorption and absorption[9–12], the dry depositional loss of particles[13–16], and organic film formation[9,17] but also serve as reaction sites that facilitate new reaction pathways and mechanisms.[18–20] There are many challenges that complicate the development of a comprehensive molecular level understanding of indoor surface processes and their impacts on indoor air quality.[6] For example, the composition of indoor surface materials are extremely complex and diverse both structurally and chemically.[2,21] These surfaces range from permeable micro- and macroscopically rough, such as painted walls, to smoother impermeable materials such as window glass. On an impermeable surface contaminant accumulation is expected to occur immediately at the air-surface interface, whereas permeable surfaces can facilitate prolonged uptake via diffusion into the underlying material matrix.

Adding on to this complexity, the exact location of the surface will determine the environmental reaction conditions (light, humidity, and temperature) and the proximity of the indoor surface.[17,22,23] For example, windows are more prone to exposure to direct and attenuated sunlight,[24] thus photochemistry may be important for these surfaces. Photochemical processes play a role in the production and regulation of oxidative gases in the indoor environment,[11,24,25] as well as SOA formation.[26] Surfaces in the presence of high levels of elevated humidity, whether periodic or maintained, can take up water vapor depending on the surface physical and chemical properties. This can lead to the formation of aqueous thin films, which are a potentially important source for gases, including nitrous acid formation, in the indoor space.[27]

As surfaces age, material accumulates through adsorption, absorption, and deposition of gases and particles, respectively. The degree of deposition to a surface obviously depends not only on the exposure time and concentrations of relevant species in air, but also the physical and chemical properties of the surface, which will also evolve with time and move away from the native surface material's original properties. For example, organic film coatings on window glass are predicted to be substantial in theoretical indoor models[9] and have been observed in high-organic loading locations such as kitchens.[17] These organic films are different from the underlying glass from

both physical and chemical perspectives. Thus, there is a need to not only study the physiochemical properties and reactivity of the bare indoor surfaces, but also how these properties transform as these surfaces age.

Window glass is a ubiquitous indoor surface, and its interaction with airborne constituents of indoor air have begun to receive more attention. Glass surfaces evolve as material accumulation[14,15,28] and film growth[9] occur at the air-surface interface, and substantial material modification is present on glass surfaces aged for weeks or even months[17]. However, these long accumulation time scales restrict the ability to understanding faster processes and interactions at the air-surface interface. Higher time resolution analyses of surfaces have been conducted but are typically carried out in laboratory environments, often coupled with theoretical simulations, targeting the mechanistic and kinetic behavior of interactions between glass surfaces or proxies with both aerosols[29] and indoor relevant organic compounds[30–32], and subsequent reactivity to common gaseous constituents of indoor air such as ozone.[18,33–35] The highly specified nature of these experiments often requires use of window glass proxies and use a smaller number of species representative of a broad family of common indoor compounds. By measuring loss behaviors of species in the airborne fraction, higher time resolution field measurements demonstrated that gas-surface partitioning play a major role in the behavior of indoor constituents.[12] However, direct surface measurements capturing the faster timescale evolution of authentic indoor surfaces has yet to be demonstrated.

To probe the progression of authentic indoor surfaces in the presence of common indoor emissions, window glass was exposed to single day cooking activities throughout the month-long HOMEChem experiments. Cooking and cleaning events during the campaign resulted in elevated levels of submicron aerosols and gaseous compounds.[36–38] Analyses of these glass surfaces reveal substantial particle deposition, dominated in number and volume by the presence of ultrafine and accumulation mode particles respectively. Spectroscopic analysis of particles shows signals associated with organic matter that is interacting with the glass surface, which may facilitate longer-term deposition of more particles onto the glass surface and subsequent increased reactions of the surface with ozone. Interpretation of spectra are supported by chamber studies demonstrating that depositions are spectroscopically mimicked by a mixture of oleic acid, a representative for fatty acids, and its byproducts following reactions with ozone. While the majority of glass surface areas examined were mostly uncoated, the overall volume of the deposited particles over a single day of exposure is equivalent to that of a film on the order of nanometers of thickness.

Methods

HOMEChem

The House Observations of Microbial and Environmental Chemistry (HOMEChem) study took place in June 2018 at the UTest house in Austin, TX. The study is described in detail by Farmer and Vance et al.[36] and included a series of scripted perturbations, including cooking and occupancy events. Of particular relevance to this surface study were two event based days that largely revolved around cooking: a simulated Thanksgiving day, in which a traditional US holiday meal was cooked for, and consumed by, 10 - 15 guests in the test house and a sequential cooking day, in which a vegetable stir-fry and rice were cooked four times throughout a day, separated by periods in which windows and doors were opened to ventilate the house. While there are differences in the overall occupancy and appliances used between the two events, time resolved size distributions show that events such as cleaning, cooking, and post-cooking decay phases dominated the degree of aerosol concentration.[37]

Online SMPS Particle Measurements

Real-time airborne particle size distributions in the size range of 10 nm – 533 nm were measured using a Scanning Mobility Particle Sizer (SMPS, TSI Inc., Shoreview, MN). The SMPS recorded one particle size distribution every five minutes. Cumulative size distributions (dN/dD_p) were generated by summing the particle counts across the entire exposure duration of each window glass sample collected for AFM and AFM-IR analyses. It is worth noting that number concentrations from the cumulative airborne size distribution cannot be exactly compared to the surface deposited number concentrations without making accurate measurements of surface deposition rates.

Window Glass Sampling

For AFM and AFM-IR analyses, window glass was cleaned using sequential methanol and water rinses, and dried in an oven. The glass was cut into 1.3 × 1.3 cm^2 pieces and exposed to several high-emission indoor activities across the HOMEChem campaign. All samples were placed vertically within the shared kitchen and living room area of the UT Test House. Individual glass slides were exposed for approximately 24 hours to one of the following emission activities: Thanksgiving (June 18, 2018), and sequential stir-fry cooking (June 6, 2018). A control was taken by exposing the sample for approximately 40 hours during the unoccupied house (June 1 – June 3, 2018) scenario.

Exact sampling dates and times are provided in **Table S1**. Samples were placed directly on top of the SMPS to minimize spatial differences in emission concentrations and any subsequent transformation or loss processes. Due to the limited time resolution of sample collection, these surface analyses probe the surfaces evolution following the cooking event as well as all other indoor events (ventilation, occupancy, etc.) throughout the exposure period. Samples were stored in sealed stainless-steel containers and shipped to UC San Diego immediately after collection for analyses. Laboratory blanks were prepared at UT Austin, stored for one month in stainless steel shipping containers, and shipped at the end of the of the campaign. Samples were stored in the dark at ambient conditions to minimize changes in surface composition and structure from condensation or photodegradation.[39]

We note that during the shipping process, higher volatility products may be lost from the surface. Thus, these offline surface analyses are limited to species that do not readily desorb from the surface passively or during the transportation process. The following results should be interpreted as a characterization of the surface evolution primarily due to lower volatility organic compounds and deposited particles. Additionally, for the smaller sized particles, these microscopy analyses cannot differentiate between either SOA formation and subsequent deposition or preferential adsorption and aggregation of SVOCs on the surface as island domains.[40,41]

For ATR-FTIR analysis, a cumulative sample collected over the last three weeks of the campaign was used. Two glass plates (25.5 cm × 30 cm) were cleaned and placed on top of the shelving unit directly above the stove. The glass plates were placed near vertically, with an approximate tilt of 5°, leaning against the wall. After the end of the campaign, the plates were collected, placed with dirty sides facing each other, wrapped in aluminum foil, sealed in a plastic bag and transported back to William & Mary for analysis. Except for time on a commercial aircraft, samples were stored frozen and were thawed before sample extraction/removal. From a slight tilt of these samples, gravitational settling is expected to enhance material accumulation relative to the fully vertical window glass samples used for microscopy analyses, and inter-sample assessments with these plates and the smaller slides for AFM-IR are strictly limited to spectroscopic comparisons.

AFM-IR Method

Samples were analyzed using a nanoIR2 (Bruker, Santa Barbara, CA) microscopy system equipped with a tunable mid-IR optical parametric oscillator laser (OPO). AFM imaging was conducted under ambient conditions at 298 K and a relative humidity (RH) of ~40% at ambient pressure to minimize particle deformation or loss. For AFM

studies, N = 8 images (30 × 30 μm^2) were collected per surface at a scan rate of 0.5 Hz and resolution of 1024 × 1024 px, using silicon nitride probes (tip radius ≤ 10 nm) with 33-77 N m^{-1} spring constant and 200-400 kHz resonant frequency in tapping mode.

For AFM-IR studies, images were collected at a scan rate of 0.5 Hz using gold-coated silicon nitride probes (tip radius ≤ 30 nm) 1-7 N m^{-1} spring constant and 75 ± 15 kHz resonant frequency in tapping mode. Photothermal infrared (PTIR) spectra were collected at tip-localized locations across the surface with a nominal spatial resolution of < 30 nm, a spectral resolution of 8 cm^{-1}, co-averaging 128 laser pulses per wavenumber. All spectra shown were taken on a single point without smoothing filters applied.

ATR-FTIR Method

Sample material was removed from the glass plate by scrapping an area of ~8 × 8 cm worth of deposited material off with a cleaned razor blade, piling it onto the ATR-FTIR crystal, and pressing it down onto the crystal with the back side of the cleaned razor blade. The bulk ATR-FTIR spectra were collected with a Shimadzu IRTracer-100 MIRacle 10 with a diamond crystal ATR probe. Spectra were acquired from 600-4,000 cm^{-1}; averaging 100 scans per spectrum; Happ-Genzel apodization was applied; and the spectra were recorded as % Absorbance. Background spectra were collected using room air.

Teflon Chamber and Laboratory Sample Preparation

A 240 L chamber made from fluorinate ethylene propylene (FEP) Teflon film (American Durafilm, MA) was used to replicate an indoor environment. Window glass substrates were cut into 2.0 × 2.0 cm^2 pieces and cleaned by sonicating for 20 minutes in both milli-Q and methanol and then subsequently dried in an oven (120°C) to remove any remaining solvent at the surface. Substrates were placed inside of the chamber and mounted vertically by a Teflon holder. 1 L/min of zero air (RH < 5%) was passed through a glass bubbler (frit size A, Ace Glass) containing 300 mL of DI water and 5 mL of oleic acid, to create oleic acid particles. The RH in the chamber was 36 ± 3% throughout the exposure. The particles then passed through a desiccator that mixed with 3 L/min of zero air and entered the chamber. A vacuum pump was set to 4 L/min at the outlet of the chamber. The glass substrates were exposed to oleic acid aerosols for about 8 hours. Clean unexposed substrates were covered and set to the side as experimental blanks. For ozone exposure, remaining oleic acid in the suspended particle or vapor phase was first

removed by letting the chamber go through 4 air exchanges. An ozone generator (Model 2000, Jelight) was used to produce 500 ppb of ozone within the chamber for 4 hours to ensure sufficient oxidation of the deposited oleic acid particles. Ozone was continuously monitored using a Model 202 Ozone Monitor (2B Technologies).

Particle and Surface Characterization

Image processing and measurements were conducted using Gwyddion™ software. In AFM/AFM-IR analyses, deposited particles were identified by setting a 4-pixel area threshold with a lower height threshold of 2.00 nm relative to the underlying glass. To account for differences in deposition morphologies, particle were sized by converting their volume (V) into their spherical equivalent volume diameter ($d_{eq,V}$) :

$$d_{eq,V} = \left(\frac{6V}{\pi}\right)^{1/3} \quad (1)$$

The particle aerodynamic diameter (d_a) is related to the volume-equivalent diameter by the formula

$d = d_{eq,V}(\rho_a/\rho\chi)^{1/2}$

$$d_a = d_{eq,V}\left(\frac{\rho C(d_{eq,V})}{\rho_0 C(d_a)}\right)^{1/2} \quad (2)$$

where ρ is the particle density, ρ_0 is the unit density and C is the slip factor.[42,43]

To assess particle morphologies, aspect ratios (AR) were determined for each identified particle by taking the ratio of maximum particle height (z_{max}) to the diameter of a circle with an equivalent projected area (A_p):

$$AR = \frac{1}{2} z_{max}\left(\frac{\pi}{A_p}\right)^{1/2} \quad (3)$$

A film equivalent thickness ($z_{eq,f}$) was calculated by taking the ratio of the cumulative volume of particles over the projected surface area for each AFM image:

$$z_{eq,f} = \frac{\sum_{i=1}^{n} V_i}{A_{proj}} \quad (4)$$

Deposition densities ($\rho_{N,surf}$) were calculated by dividing the total number of particles measured by the overall surface area (900 μm^2 / image). Values are expressed as per cm^2 for more convenient macroscopic comparisons.

Changes in surface area are calculated by taking the difference between the measured and projected surface area per AFM image:

$$\Delta SA = SA - SA_0 \quad (5)$$

The measured surface area (SA) includes the additional surface area provided by the additional dimension of topography, while the projected surface area (SA_0) is the two-dimensional area imaged. A perfectly flat surface should have equal measured and projected surface areas, and subsequently a null change in surface area. Surface roughness values were calculated using root mean square roughness (R_q) per height image, which is readily calculated from an n pixel height images using the height per pixel (z_p) and mean height ($\bar{z}$):

$$R_q = \sqrt{\frac{1}{n}\sum_{p=1}^{n}\left(z_p - \bar{z}\right)^2} \quad (6)$$

Surface coverage by particles was calculated by taking the ratio of the summed particle surface area (SA_i) to the total surface area per AFM image:

$$\theta = \frac{\sum_{i=1}^{n} SA_i}{SA} \quad (7)$$

Modeling Methods and Parameters

Size-resolved particle deposition rates were analyzed using the Lai-Nazaroff model (2000)[29] that estimated particle deposition onto a smooth surface considering size-dependent Brownian and turbulent diffusion and gravitational settling. These modeled results were compared to the glass samples from AFM analyses, which were

placed vertically. Thus, gravitational settling was considered negligible. The local airflow condition near the glass surface was approximated by using friction velocity (u*). The typical range of friction velocity for the indoor environment is 0.3 to 3.0 cm/s, based on experimental and modeling studies.[44] During the experiments, the central mixing fan circulated indoor air in the house every 7.5 min (eight house volume of air per hour); therefore, to calculate particle deposition onto the vertical glass surface with the sample area of 7200 μm^2, we used two relatively high values of friction velocity: 1) 1 cm/s which represents the typical indoor friction velocity and 2) 3 cm/s as an upper boundary limit with a relatively high indoor air mixing condition. Particle sizes were restricted to diameters between 10 – 532 nm, which were the size ranges that overlapped between the AFM and SMPS measurements. Using the size-dependent deposition velocities with airborne concentrations, the time- and size-resolved particle concentrations on the glass surface were calculated for the Thanksgiving cooking and stir-fry events. Comparisons were also made between the measured and modeled 24-h integrated particle concentrations (size-resolved) for those two measurement events.

Results and Discussion

AFM Surface Measurements

Representative AFM images of particle depositions on window glass are shown in **Figure 1**, where enhanced particle loading is observed in both cooking events. Two controls were employed to look at the relative enhancement of particle deposition. A material blank was exposed to zero emissions, while the unoccupied

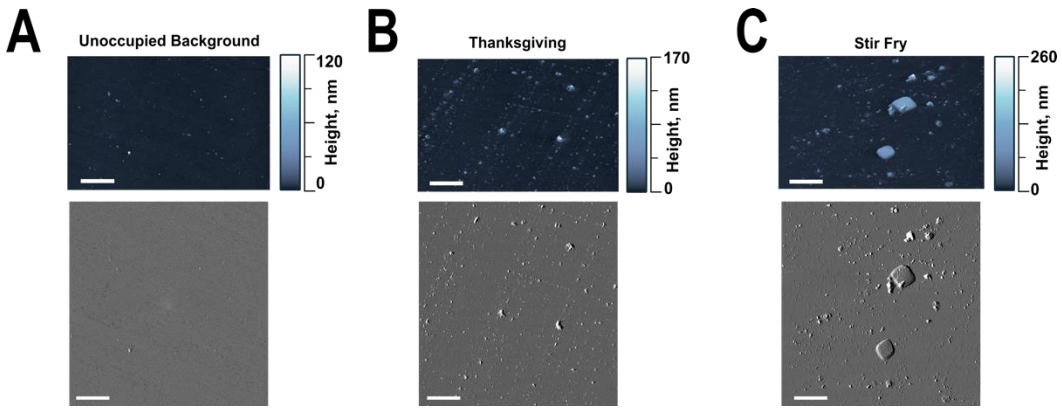

Figure 1. 3D AFM height images (upper) and corresponding AFM amplitude images (below) of the glass surfaces exposed to different activities with scale bars set to 5 µm. Note height scales increase from 120 to 260 nm across the images of the different activities.

background served as an event control wherein the glass samples were left to interact with the ambient room air in the absence of any indoor activities. Relative to the material blank, the unoccupied-glass was far from clean, with approximately four-fold more particles (**Figure S1**). These deposited particles can be attributed to infiltration and ventilation of outdoor air which will introduce ambient aerosols to the indoor environment, in combination with emissions of semi-volatile gaseous compounds from building materials and furnishings.[45] The airborne size distribution from the unoccupied background is shown in **Figure S2**. Prior to collection, the oven was running to remove residual material, resulting in an enhancement of PM levels during the collection period. However, even with the elevated PM levels in the unoccupied background, both cooking conditions produced an enhancement in particle deposition across all sizes (**Figure 1)**.

As measured by AFM images, the Thanksgiving and stir-fry events resulted in an overall density of 6.7 $\times 10^8$ and 4.3 $\times 10^8$ particles/cm^2 respectively. Size-segregated particle deposition densities as a function of airborne particle number concentrations for each event are shown in **Figure 2**. As expected, the $\rho_{N,surf}$ increases with the

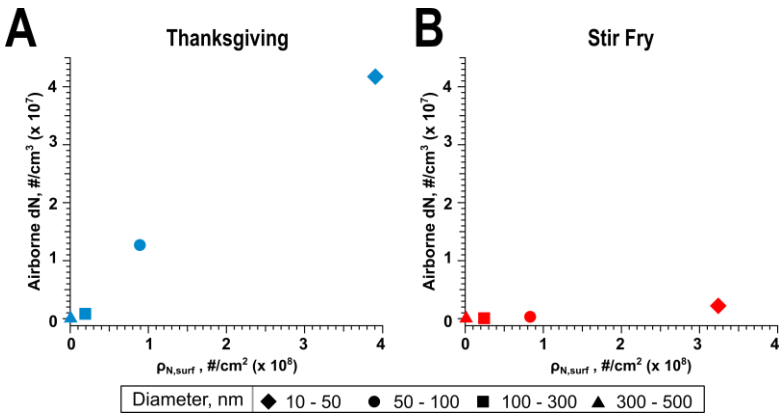

Figure 2. Surface deposition densities as a function of cumulative airborne PM number concentrations for A) Thanksgiving (blue) and B) stir fry (red) events for four particle size bins: 10 – 50 nm, 50 – 100 nm, 100 – 300 nm, and 300 – 500 nm diameters (D_p and $d_{equiv,V}$ for airborne and surface measured diameters respectively) .

airborne concentration in both cases, and the majority of deposited particles are observed in the smaller size bins. However, the densities of surface deposited particles were comparable, if not elevated, from the stir fry event in all size bins. Even in smallest size bin of 10 -50 nm particles, there are comparable deposition densities on the surface – 3.9 $\times 10^8$ and 3.2 $\times 10^8$ particles/cm^2 in the Thanksgiving and stir fry event respectively, but over an order of magnitude higher particles were measured in the airborne fraction during the Thanksgiving event.

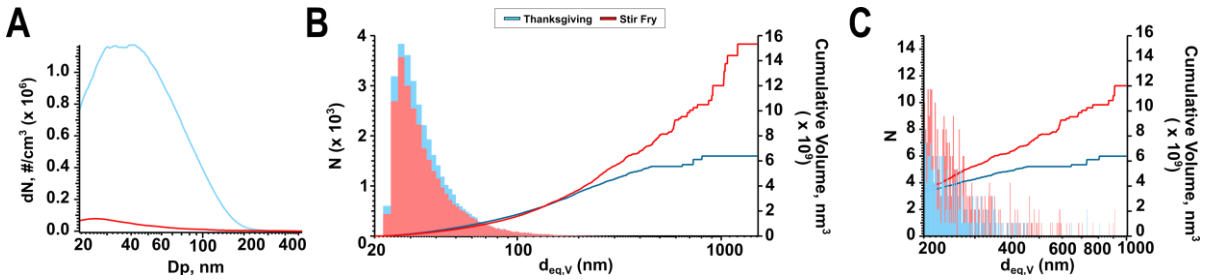

Figure 3. A) Cumulative airborne size distributions from stir fry (red) and Thanksgiving (blue) events. B) Surface deposited number and cumulative volume size distributions from stir fry and Thanksgiving events, with a zoom in of the larger submicron sized particles in panel C).

Cooking events size distributions of the airborne PM from the Thanksgiving and stir fry cooking events are shown in **Figure 3A**, with corresponding surface deposited size and cumulative volume distributions in **Figure 3B** and **3C**. The Thanksgiving event produced higher levels of particles in terms of both mass and number, especially for the particles under 200 nm. However only a slight increase in the deposition of ultrafine sized particles is observed, with a decrease in both accumulation-mode and supermicron sized deposited particles relative to the stir fry event.

In all samples, the predominant fraction of deposited particles by number is within the ultrafine size regime ($d_{equiv,V}$ < 100 nm). These results are expected as the ultrafine particles dominated the airborne concentration. While we cannot distinguish any preferential surface adsorption of SVOCs in aggregate structures, these results suggest that impermeable flat indoor surfaces like window glass can actively partake in removing ultrafine particles via deposition. Ultrafine particles emitted from these common household events are difficult to regulate and monitor, and a comprehensive understanding of their surface interaction processes are important for gauging the capability of indoor surfaces to remove these particles from the air.

While the majority of deposited particles by number occur in the ultrafine size range, these smaller particles are not necessarily responsible for most of the material modification of indoor surfaces. Relative to the unoccupied background, deposition of the larger particles (100 nm < $d_{equiv,V}$ < 1000 nm) are heightened during the Thanksgiving, and stir fry events by 208 and 265% respectively. As expected, the overall volume (and subsequent mass) loading of these surfaces due to deposition is dominated by the particles with $d_{equiv,V}$ greater than 100 nm. These larger particles comprised 89% and 71% of the depositional material in the stir fry and Thanksgiving events respectively. Thus, events with emissions of larger particles (such as cooking) are expected to produce the most organic material loading on surfaces.

Comparison with Deposition Models

Particle deposition requires transport from air to a surface and then adhesion (stick) to the surface upon collision. Transport to a surface depends on mixing conditions above the surface and the size of the boundary layer adjacent to the surface. Under otherwise similar air velocities above a surface, a surface with a smaller characteristic length, e.g., small glass specimens versus an entire wall, will have a much smaller average boundary layer thickness and hence a smaller transport resistance for particle interactions with a surface.[46] As such, it is expected that for the small glass specimens used in this study the friction velocity should have been relatively large and transport resistance relatively small. If this was the case, the effects of adhesion resistance were magnified.

A comparison of the field measurements with the Lai-Nazaroff deposition model for particles onto smooth surfaces is shown in **Figure 4A** and **4B** for the Thanksgiving and stir fry events, respectively. The model itself accounts for turbulent diffusion and Brownian motion on a smooth vertical surface. Size-resolved particle deposition was modeled for the size range of 10-532 nm that overlaps between the SMPS and AFM measurements. We see good agreement between the model and measured values for particle deposition in the Thanksgiving cooking event wherein particles under 75 nm are predicted well with a surface friction velocity of 3 cm/s. The calculated ranges for deposition velocity were 6.98 $\times 10^{-5}$ to 5.24 $\times 10^{-3}$ cm/s (u*= 3 cm/s) and 2.0 $\times 10^{-5}$ to 1.75 $\times 10^{-3}$ cm/s (u*= 1 cm/s). These deposition velocities are slightly lower but comparable to previously reported deposition velocities of fine-

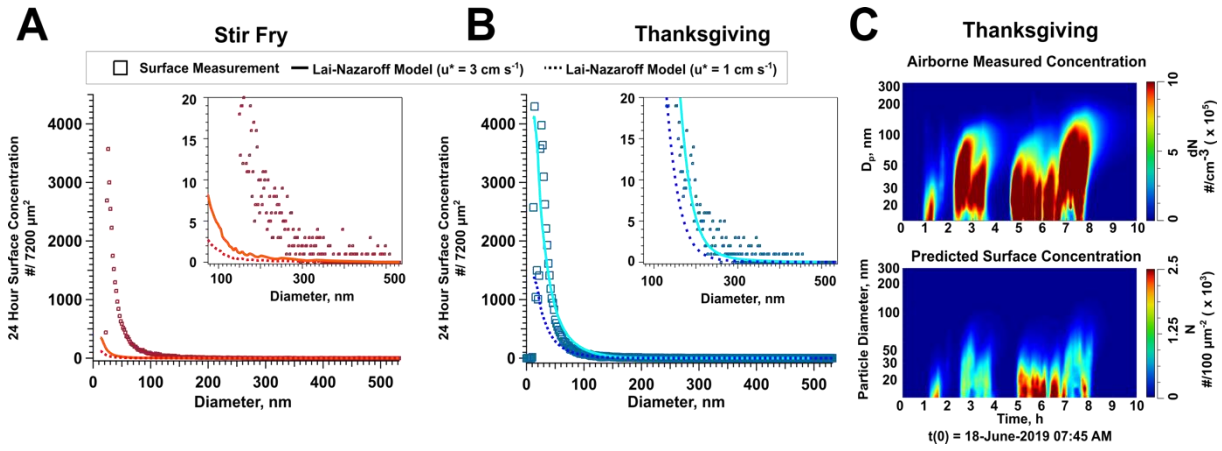

Figure 4. Comparison between the size dependent deposition (square markers) measured by AFM and predicted by the Lai-Nazaroff model with surface friction velocity of 1 (dashed line) and 3 (solid line) cm/s for the A) Thanksgiving and B) stir fry events. Insets show a zoom in of the larger sized particles. Panel C shows the model predicted surface concentrations using the time resolved airborne size distributions from the SMPS.

mode particles onto vertical surfaces, where reported deposition velocities ranged from 5 $\times 10^{-3}$ to 2 $\times 10^{-5}$ cm/s.[29,47–52] The detailed simulated time- and size-resolved particle depositions for the Thanksgiving event are shown in

Figure 4C, wherein the elevated levels of deposition are predicted to be around the 13:00 – 15:00 (t = 5 – 6.5hr) and 15:30 – 16:00 (t = 7 – 7.5 hr), which corresponded to the Thanksgiving preparation and cooking events, large sources for primary and secondary aerosols. Interestingly, even with a surface friction velocity of 3 cm/s, the model vastly under predicts the deposition observed in the stir fry scenario, in which we observe roughly an order of magnitude more deposited particles than predicted.

Several factors may have contributed to discrepancies between modeled and measured levels of particle deposition. It is possible, for example, that the stir-fry event produced lower volatility particles or compounds that had a higher affinity to adhere to window glass, thereby resulting in lower adhesion resistance and enhanced particle deposition. Specific surface chemical interactions are not considered in the current deposition models nor are issues related to surface adhesion forces, which dictate whether particles "stick" or "bounce" after contact. It is also possible that transport resistance was lower for stir-fry events than for the Thanksgiving event due to greater air speeds adjacent to glass surfaces. Measurements of air speed above surfaces were not completed during experiments and so it is not possible to confirm whether lower transport resistance occurred during experiments. These discrepancies and findings highlight the importance of probing in more detail the physiochemical interactions between indoor surface and particle emissions. Cooking events release considerable amounts of organics, highly diverse in composition,[53] from both any oil splash and cooking processes. Emissions of primary particles from cooking and formation of secondary particles from condensation of semi- and low-volatility gases on new or existing particles enhances particle mass in to the indoor air space.[54,55] Primary emissions from the cooking processes are likely the main driving factor causing enhanced levels of organic aerosols in the indoor air and thus deposited on window glass surfaces. [36,56]

Particle Viscosity

Shown in **Figure 5** are plots of the particle height-to-base aspect ratio (AR) as a function of their spherical volume equivalent diameter. Briefly, a higher aspect ratio is indicative of little to no deformation upon deposition and tends towards more viscous solid particles, whereas low aspect ratios are found in flat, highly spread particles, suggestive of liquid or semi-solid particles.[57] While the final morphology of the deposited particles will depend on complex interactions arising from surface-particle interactions and other physiochemical properties of the particle and surface, the size-specific provide qualitative insight into the viscosity of different particle types.

Due to changes in environmental conditions, some evaporation of water vapor and higher volatility organic compounds is to be expected during shipping and storage, which can alter the phase state, viscosity, and morphology of the particles.[58–62] These discrepancies can be addressed by future investigations into different environmental conditions focused on the reversibility of different VOCs and water vapor uptake. Nearly all deposited particles were flat - 99.9% and 99.6% of particles under an AR of 0.165 in the stir fry and Thanksgiving events respectively. This large degree of spreading is typically indicative of less viscous liquid-like organic particles.[58] It is conceivable that the large predominance of highly spread particles could have arisen due to higher viscosity particles bouncing off of the surface. Even in higher pressure impactor systems, aerosols that collide with substrates and collection surfaces can either collide and remain on the surface or bounce back off into the headspace.[63] The depositions observed in this study are more representative of the deposition and adsorption part of the overall particle-surface interactions. While AR analyses provide some insight into the phase state of deposited particles, these measurements do not provide any metric directly translatable into actual values of the particle viscosity or relevant forces such as adhesion or surface tension. These parameters can be accessed with techniques such force spectroscopy[58,64,65] and

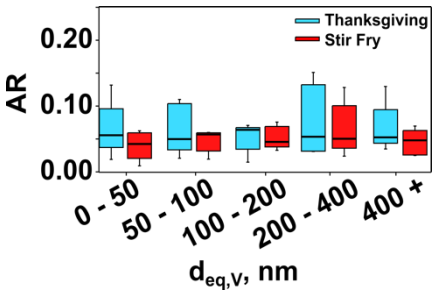

Figure 5. Box plots of particle aspect ratio as a function spherical equivalent diameter for all deposited particles taken from the N=8 AFM images (30 × 30 μm^2) per event (Thanksgiving – blue and stir fry- red). Boxes show the 25th and 75th percentiles, and lines show 10 and 90th percentile respectively.

tensiometry[66,67], and such measurements are needed to properly address the impact of viscosity on deposition model accuracy.

Spectroscopic Characterization of Deposited Particles

A comparison of spectra taken from different deposited material on window glass is shown in **Figure 6**. Tip-localized PTIR spectra shown were taken on deposited particles from a day of stir-frying events in HOMEChem. A reference PTIR spectra was also taken on a film that developed on window glass exposed to a residential kitchen environment for one month, separate from the HOMEChem campaign. The ATR-FTIR spectra shown in black are taken from material extracted from window glass samples exposed to the last three weeks of HOMEChem activity. Spectrally, there is strong overlap between spectra taken from the two long-term exposed glass surfaces. The glass from HOMEChem (ATR-FTIR) exposed for three weeks and 1-month glass exposed to the kitchen, with a strong ν(C=O) peak around 1742 cm^{-1}. It is important to note that the ATR-FTIR spectra show the spectral signatures of species that have been scraped off the window glass. However, there is still strong spectral overlap with the PTIR spectra from the 1-month exposed kitchen glass, wherein analyses of deposited particles can be conducted without disturbing them from their interactions with the underlying glass. In comparison, in the glass

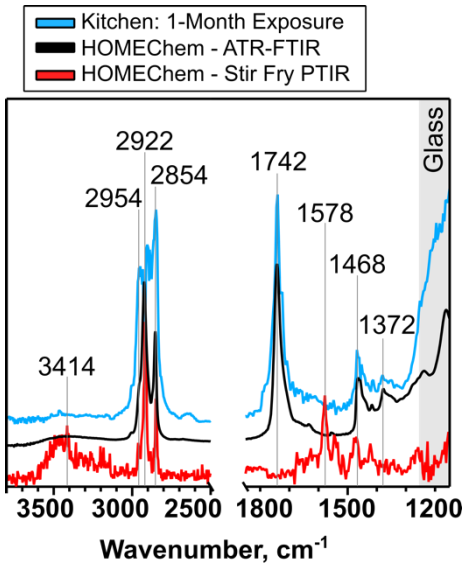

Figure 6. Comparison of PTIR spectra taken from a film coating on kitchen glass from 1 month old kitchen glass outside of the HOMEChem campaign (blue), ATR-FTIR spectrum of acetonitrile-extracted material from 3-week exposed glass during HOMEChem (black), and PTIR spectra of deposited particles on window glass from a single day of exposure to stir fry cooking (red).

exposed to just a single day of sequential stir fry events, there is a noticeable peak around 3414 cm^{-1} from OH stretching motions. In addition, there is no obvious peak present in the spectral range associated with a carbonyl stretch, v(C=O) around 1700 cm^{-1}, but instead a predominant peak at 1578 cm^{-1}, which we are attributing to the asymmetric stretch of carboxylate and potentially some unreacted alkenyl functional groups. The absence of this mode in the longer-term exposed window glass may be indicative of longer time-scale processes displacing surface-bound compounds or changing the speciation of deposited materials via acid-base reactions.

To confirm the organic nature of the deposited materials from both cooking events, tip-localized IR spectra were collected on deposited particles from the corresponding events, with representative particles shown in **Figure 7**. The high spatial resolution[68,69] of the AFM-IR enables spectroscopic analyses of these submicron particles on a single particle basis.[70] Spectra from deposited particles reveal that these particles contain carboxylate moieties, as indicated by the strong $v_{as}(COO^-)$ and $v_s(COO^-)$ modes around 1570 and 1430 cm^{-1} respectively, with slight variations in the overall curve shape and peak positions. Additional spectroscopically characterized particles are shown in **Figure S4** and **S5** wherein the most common spectra in analyzed particles are carboxylate-rich species. Low exposure time and lack of ambient oxidants would allow some alkenyl groups to persist within depositions, and if so, v(C=C) modes can be expected to contribute to the peak observed around 1610 cm^{-1}. The presence of these

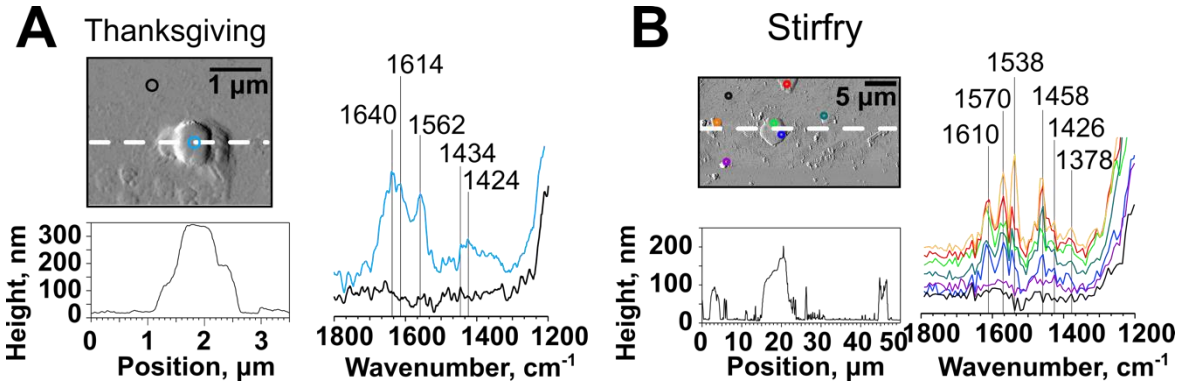

Figure 7. AFM-IR spectra and the corresponding AFM images (with color marked locations) of deposited particles from A) Thanksgiving, and B) stir fry events. Spectral features of these particles show deprotonated organics, as indicated by the $v_{as}(COO^-)$ and $v_s(COO^-)$ modes around 1580 and 1450 cm^{-1} respectively.

species may be caused by non-acidic environments at the aqueous silica interface.[71,72] Alternatively, they may arise due to bonding with the silica surfaces in window glass[73]. In the spectra shown, particles also show bands around

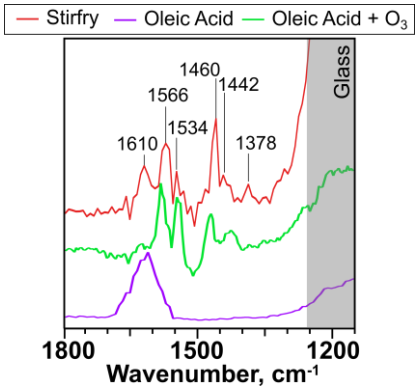

Figure 8. Spectral comparison between PTIR spectra taken on depositions from the stir fry event and laboratory mimetics generated in a Teflon chamber – oleic acid particles in green and oleic acid particles oxidized with ozone in purple.

1400 cm^{-1} that can be associated with δ(CH3)/ δ(CH_2) modes. A spectral comparison of the stir fry deposited particles with some laboratory generated surfaces is shown in **Figure 8**, wherein oleic acid particles, representing fatty acids which are commonly emitted during cooking[53], are used as a laboratory proxy for cooking organic aerosols.

We observe that there is fairly good overlap of the vibrational modes associated with the functional groups from a mixture of oxidized and unoxidized fatty acids. Some of the major products of oleic acid oxidation through ozone are nonyl aldehyde (nonanal), nonanoic acid, among many other carbonyl containing compounds. Previous studies reported sharp increases in nonanal emissions over time from material placed in a kitchen environment[17] and sequentially exposed to ozone.[74] Unreacted oleic acid particles deposited on window glass gives rise to a single detected mode at 1610 cm^{-1}. Surprisingly, even with the oxidation of oleic acid we do not observe the vibrational modes associated with protonated carboxylic acids or other carbonyl groups that we expect around 1700 cm^{-1}. Rather, we observe the formation of a pair of doublets corresponding to the asymmetric and symmetric carboxylate stretches around 1566, 1534 cm^{-1} and 1469, 1442 cm^{-1} respectively. The presence of a carboxylic acid group could potentially be important for enabling long term binding of the particle onto the surface, allowing them to remain adsorbed for longer durations of time. These results suggest the potential importance of surface-particle chemical interactions, the influence surface acidity on deposition speciation, and the availability of binding moieties on the surface to facilitate particle deposition. The deposited particle from the Thanksgiving event shows similar carboxylate modes present around 1610, 1562 and 1424 cm^{-1}. However, an additional more intense mode is observed around 1640 cm^{-1}. Narrowing down the exact family of molecules responsible for this absorbance feature is beyond the capabilities of these analyses. However, potential contributors are unreacted alkenyl moieties from of

unsaturated organics, amides which have been detected from meat cooking,[53] or from the O-H bends of hydroxyl containing species like absorbed water.[75] Nebulized water-soluble extracts from the larger glass plate have reported elemental ratios O/C and H/C of 0.21 and 1.8 respectively[36], consistent within the reported range of typical O/C ratios for cooking organic aerosols measured in both residential kitchens and produced and aged in chambers. The collection period of the extract is on the order of weeks, and thus are susceptible to reactions with light or reactive gases. Chamber and laboratory studies looking at elemental ratios of cooking organic aerosols found that unreacted emissions were typically found with an O/C around 0.1. Upon aging in the presence of ozone or UV light, O/C ratios increased to around 0.2 to 0.3.[76,77] These results further suggest the surface deposited particles samples have been aged, however, narrowing down the exact source, location (surface deposited or aerosol phase), and mechanism for this aging (oxidant, photochemical, or even degradation from high cooking temperatures) is beyond the current capabilities of these analyses. Future investigations are needed to investigate the influence of particle composition on deposition, and subsequent physiochemical properties of indoor surfaces such as photochemical reactivity, water uptake, and gas-species partitioning. In addition to how these properties change upon surface aging under realistic indoor conditions.

Impact of Deposition on Surface Properties

A few surface properties of interest calculated using the same AFM images (N = 8) as above are summarized in **Table 1**. These properties include surface roughness, change in surface area, equivalent film thickness, and surface coverage. Properties such as film equivalent thickness and roughness can be heavily skewed by the presence of supermicron particles, which could have originated from deposition of dust or glass shards during the substrate cleaving. Because these offline analyses cannot discriminate the origin of these large particles, calculated values shown in **Table 1** do not include corrections for the presence of these large particles. These larger particles were present in only one image from both the unoccupied background (**Figure S3**) and laboratory blank, resulting in relatively large errors. However, a comparison of the surface properties is summarized in **Table S2** with and without the corresponding images.

Table 1. Surface properties of window glass exposed to various indoor events throughout HOMEChem measured by AFM, with standard deviations shown in parentheses.

Event	R_q, nm	ΔSA, μm^2	$z_{eq,film}$, nm	θ , %
Laboratory Blank	6.0 (8.5)	1.0(1.2)	0.4(0.7)	1.8(1.2)
Unoccupied Background	7.8(13.2)	1.4(1.2)	0.8(1.2)	6.0(3.9)
Thanksgiving	4.9(2.1)	2.7(0.7)	0.9(0.5)	10.9(1.9)
Stir Fry	11.2(5.3)	3.3(2.0)	2.1(1.1)	18.5(5.6)

R_q: root mean square roughness (Eq. 6)

ΔSA: change in surface area (Eq. 4)

$z_{eq,film}$: film equivalent thickness (Eq. 5)

θ : surface coverage by deposited material taller than 2 nm in height (Eq. 7)

For all properties measured, the stir fry event saw the larger departure from the control. For comparisons with current models and studies on indoor film formation, the total volume of the particles is projected as a film of uniform thickness onto the surface area of each image. In the unoccupied control, due to the high levels of adsorbed particles there is a 0.8 ± 1.2 nm thick film. However, this value is noticeably enhanced following the stir fry (2.1 ± 1.1 nm) event and slightly elevated for the Thanksgiving (0.9 ± 0.5 nm) event. Under the assumption that the deposited particles are 50% organic, this would still correlate to a 1.2 nm equivalent film of organics in the stir fry event, suggesting that in high emission events like cooking, particle mass loading onto indoor surfaces will play a major role in altering the organic coating of the indoor emissions.

Surface coverage values (**Table 1**) provide further insight into deposition heterogeneity across the surfaces, where regions of bare glass and particle-coated glass are present. Coverage in the background sample was approximately 6 ± 4%. Expectedly, the largest deviation from the blank occurred in the stir fry event (8 ± 6 %) and Thanksgiving produced moderate coverage (11 ± 2%), but overall much of the surface was left uncovered. Low surface coating is unsurprising as the samples were only exposed for a single day event. Surface roughness increased marginally relative to the unoccupied scenario (7.8 ± 13.2 nm) in the stir fry (11.2 ± 5.3 nm) but decreased in the Thanksgiving event (4.9 ± 2.1 nm). Similarly, changes in surface area for the stir fry and Thanksgiving scenarios

were small, 3.3 ± 2.0 μm^2 and 2.7 ± 0.7 μm^2 respectively. These findings are consistent with a recent study which found that increases in surface area and roughness were most drastically impacted by larger sized particles.[17] In all emission cases, particle deposition was predominantly ultrafine in terms of number, and subsequently, changes to surface area and roughness are relatively low.

Conclusion

Common indoor activities like cooking contribute high levels of particle emissions that subsequently deposit onto indoor surfaces. These particles are largely organic as suggested by their deposited morphologies and spectral signatures. Studying the evolution of these surfaces due to single events provides a more complete picture of how a specific set of activities contributes towards the evolution of indoor surfaces. Coexistence of coated and bare surface creates a more complex picture that must be considered when accurately modeling these indoor surfaces. Depending on the coverage, aged surfaces can behave like a mixture of the native surface and surface-bound particulate matter, and this ratio between bare and coated regions can vary over time. These surface-based analyses provide a more comprehensive picture, which can be used to guide modelers on which properties contribute towards more long-term evolution of surfaces. Additional studies are needed to expand the existing knowledge base indoor surface chemistry towards different types of surfaces, such as painted walls and carpet, where nanoscale imaging techniques may be challenged by the roughness, softness, and porous nature of these surfaces. Moreover, characterizing these surfaces is only part of the picture, and future studies are required to understand how these surfaces and the constituents that deposit on them undergo reaction chemistry in indoor environments. What we observe from this study is that even just considering a single event indoors such as cooking with window glass, there remains complexities and challenges with some suggestions of interesting underlying chemical interactions not captured in current deposition models. A single day of simulated exposure produces large amounts of material loading onto these surfaces, the nature of which will depend on the type surface in addition to the type and duration of the details of the different activities, leaving many challenges as well as opportunities in unraveling the complexities associated with the chemistry and composition of indoor surfaces.

Conflicts of Interest

There are no conflicts of interest to declare.

Acknowledgements

The authors gratefully acknowledge the support of the Alfred P. Sloan Foundation (G-2020-12675, G-2017-9944) and the National Science Foundation Graduate Research Fellowship Program (DGE1650112).

References

1 N. E. Klepeis, W. C. Nelson, W. R. Ott, J. P. Robinson, A. M. Tsang, P. Switzer, J. V. Behar, S. C. Hern and W. H. Engelmann, *J. Expo. Anal. Environ. Epidemiol.*, 2001, **11**, 231–252.

2 C. J. Weschler, *Indoor Air*, 2011, **21**, 205–218.

3 C. J. Weschler and N. Carslaw, *Environ. Sci. Technol.*, 2018, **52**, 2419–2428.

4 C. J. Weschler and H. C. Shields, *Environ. Sci. Technol.*, 1996, **30**, 3250–3258.

5 D. Dai, A. J. Prussin, L. C. Marr, P. J. Vikesland, M. A. Edwards and A. Pruden, *Environ. Sci. Technol.*, 2017, 51, 7759–7774.

6 W. W. Nazaroff and A. H. Goldstein, *Indoor Air*, 2015, **25**, 357–361.

7 S. Gligorovski and J. P. D. Abbatt, *Science*, 2018, **359**, 632–633.

8 C. J. Weschler and H. C. Shields, *Atmos. Environ.*, 2003, **37**, 5621–5631.

9 C. J. Weschler and W. W. Nazaroff, *Indoor Air*, 2017, **27**, 1101–1112.

10 C. J. Weschler and W. W. Nazaroff, *Environ. Sci. Technol.*, 2014, **48**, 1230–1237.

11 J. P. S. Wong, N. Carslaw, R. Zhao, S. Zhou and J. P. D. Abbatt, *Indoor Air*, 2017, **27**, 1082–1090.

12 C. Wang, D. B. Collins, C. Arata, A. H. Goldstein, J. M. Mattila, D. K. Farmer, L. Ampollini, P. F. DeCarlo, A. Novoselac, M. E. Vance, W. W. Nazaroff and J. P. D. Abbatt, *Sci. Adv.*, , DOI:10.1126/sciadv.aay8973.

13 Q.-T. Liu, R. Chen, B. E. McCarry, M. L. Diamond and B. Bahavar, *Environ. Sci. Technol.*, 2003, **37**, 2340–2349.

14 B. Lam, M. L. Diamond, A. J. Simpson, P. A. Makar, J. Truong and N. A. Hernandez-Martinez, *Atmos. Environ.*, 2005, **39**, 6578–6586.

15 C. M. Butt, M. L. Diamond, J. Truong, M. G. Ikonomou and A. F. H. Ter Schure, *Environ. Sci. Technol.*, 2004, **38**, 724–731.

16 G. Bekö, G. Morrison, C. J. Weschler, H. M. Koch, C. Pälmke, T. Salthammer, T. Schripp, A. Eftekhari, J. Toftum and G. Clausen, *Indoor Air*, 2018, **28**, 247–257.

17 V. W. Or, M. R. Alves, M. Wade, S. Schwab, R. L. Corsi and V. H. Grassian, *Environ. Sci. Technol. Lett.*, 2018, **5**, 514–519.

18 R. Alwarda, S. Zhou and J. P. D. Abbatt, *Indoor Air*, 2018, **28**, 655–664.

19 D. B. Collins, R. F. Hems, S. Zhou, C. Wang, E. Grignon, M. Alavy, J. A. Siegel and J. P. D. Abbatt, *Environ. Sci. Technol.*, 2018, **52**, 12419–12427.

20 M. Sleiman, L. A. Gundel, J. F. Pankow, P. Jacob, B. C. Singer and H. Destaillats, *Proc. Natl. Acad. Sci.*, 2010, **107**, 6576–6581.

21 C. Bi, Y. Liang and Y. Xu, *Environ. Sci. Technol.*, 2015, **49**, 9674–9681.

22 S. C. Lee, S. Lam and H. Kin Fai, *Build. Environ.*, 2001, **36**, 837–842.

23 E. Abt, H. H. Suh, P. Catalano and P. Koutrakis, *Environ. Sci. Technol.*, 2000, **34**, 3579–3587.

24 S. F. Kowal, S. R. Allen and T. F. Kahan, *Environ. Sci. Technol.*, 2017, **51**, 10423–10430.

25 M. Mendez, N. Blond, P. Blondeau, C. Schoemaecker and D. A. Hauglustaine, *Atmos. Environ.*, 2015, **122**, 521–530.

26 T. Liu, Z. Wang, D. D. Huang, X. Wang and C. K. Chan, *Environ. Sci. Technol. Lett.*, 2018, **5**, 32–37.

27 S. M. Duncan, K. G. Sexton and B. J. Turpin, *Indoor Air*, 2018, **28**, 198–212.

28 X. Zhang, M. L. Diamond, M. Robson and S. Harrad, *Environ. Sci. Technol.*, 2011, **45**, 3268–3274.

29 A. C. K. Lai and W. W. Nazaroff, *J. Aerosol Sci.*, 2000, **31**, 463–476.

30 Y. Fang, P. S. J. Lakey, S. Riahi, A. T. McDonald, M. Shrestha, D. J. Tobias, M. Shiraiwa and V. H. Grassian, *Chem. Sci.*, 2019, **10**, 2906–2914.

31 Y. Fang, S. Riahi, A. T. McDonald, M. Shrestha, D. J. Tobias and V. H. Grassian, *J. Phys. Chem. Lett.*, 2019, **10**, 468–473.

32 Y. Fang, D. Lesnicki, K. J. Wall, M. P. Gaigeot, M. Sulpizi, V. Vaida and V. H. Grassian, *J. Phys. Chem. A*, 2019, **123**, 983–991.

33 H. M. Hung and C. W. Tang, *J. Phys. Chem. A*, 2010, **114**, 13104–13112.

34 H. Schwartz-Narbonne, C. Wang, S. Zhou, J. P. D. Abbatt and J. Faust, *Environ. Sci. Technol.*, 2019, **53**, 1217–1224.

35 Z. Zhou, S. Zhou and J. P. D. Abbatt, *Environ. Sci. Technol.*, 2019, **53**, 12467–12475.

36 D. K. Farmer, M. E. Vance, J. P. D. Abbatt, A. Abeleira, M. R. Alves, C. Arata, E. Boedicker, S. Bourne, F. Cardoso-Saldaña, R. Corsi, P. F. Decarlo, A. H. Goldstein, V. H. Grassian, L. Hildebrandt Ruiz, J. L. Jimenez, T. F. Kahan, E. F. Katz, J. M. Mattila, W. W. Nazaroff, A. Novoselac, R. E. O'Brien, V. W. Or, S. Patel, S. Sankhyan, P. S. Stevens, Y. Tian, M. Wade, C. Wang, S. Zhou and Y. Zhou, *Environ. Sci. Process. Impacts*, 2019, **21**, 1280–1300.

37 S. Patel, S. Sankhyan, E. K. Boedicker, P. F. DeCarlo, D. K. Farmer, A. H. Goldstein, E. F. Katz, W. W. Nazaroff, Y. Tian, J. Vanhanen and M. E. Vance, *Environ. Sci. Technol.*, , DOI:10.1021/acs.est.0c00740.

38 J. M. Mattila, P. S. J. Lakey, M. Shiraiwa, C. Wang, J. P. D. Abbatt, C. Arata, A. H. Goldstein, L. Ampollini, E. F. Katz, P. F. Decarlo, S. Zhou, T. F. Kahan, F. J. Cardoso-Saldaña, L. H. Ruiz, A. Abeleira, E. K. Boedicker, M. E. Vance and D. K. Farmer, *Environ. Sci. Technol.*, 2020, **54**, 1730–1739.

39 O. Laskina, H. S. Morris, J. R. Grandquist, A. D. Estillore, E. A. Stone, V. H. Grassian and A. V. Tivanski, *Environ. Sci. Technol.*, 2015, **49**, 13447–13453.

40 E. R. Garland, E. P. Rosen and T. Baer, in *ACS Symposium Series*, ed. R. R. Valsara Kalliat T., Kommalapati, American Chemical Society, 2009, vol. 1005, pp. 13–29.

41 E. R. Garland, E. P. Rosen, L. I. Clarke and T. Baer, *Phys. Chem. Chem. Phys.*, 2008, **10**, 3156–3161.

42 W. C. Hinds, *Properties, Behavior, and Measurement of Airborne Particles*, Wiley-Interscience, 2nd edn., 1999, vol. 14.

43 M. Kerker, *Aerosols and Atmospheric chemistry : the kendall award symposium honoring.*, Elsevier Science, 1st edn., 1972.

44 T. Hussein, A. Hruška, P. Dohányosová, L. Džumbová, J. Hemerka, M. Kulmala and J. Smolík, *Atmos. Environ.*, 2009, **43**, 905–914.

45 K. Kristensen, D. M. Lunderberg, Y. Liu, P. K. Misztal, Y. Tian, C. Arata, W. W. Nazaroff and A. H. Goldstein, *Indoor Air*, 2019, **29**, 645–655.

46 G. C. Morrison, P. Zhao and L. Kasthuri, *Atmos. Environ.*, 2006, **40**, 3677–3685.

47 J. D. Sinclair, L. A. Psota-Kelty and C. J. Weschler, *Atmos. Environ.*, 1988, **22**, 461–469.

48 J. D. Sinclair, L. A. Psota-Kelty, C. J. Weschler and H. C. Shields, *Atmos. Environ. Part A, Gen. Top.*, 1990, **24**, 627–638.

49 W. W. Nazaroff, M. P. Ligocki, T. Ma and G. R. Cass, *Aerosol Sci. Technol.*, 1990, **13**, 332–348.

50 B. Zhao, C. Chen and Z. Tan, *J. Aerosol Sci.*, 2009, **40**, 29–43.

51 N. P. Gao and J. L. Niu, *Atmos. Environ.*, 2007, **41**, 3862–3876.

52 D. Rim, J. Il Choi and L. A. Wallace, *Environ. Sci. Technol.*, 2016, **50**, 10031–10038.

53 Y. Zhao, M. Hu, S. Slanina and Y. Zhang, *Atmos. Environ.*, 2007, **41**, 8163–8171.

54 K. L. Abdullahi, J. M. Delgado-Saborit and R. M. Harrison, *Atmos. Environ.*, 2013, 71, 260–294.

55 T. Liu, Z. Li, M. Chan and C. K. Chan, *Atmos. Chem. Phys.*, 2017, **17**, 7333–7344.

56 F. Klein, U. Baltensperger, A. S. H. Prévôt and I. El Haddad, *Indoor Air*, 2019, **29**, 926–942.

57 J. P. Reid, A. K. Bertram, D. O. Topping, A. Laskin, S. T. Martin, M. D. Petters, F. D. Pope and G. Rovelli, *Nat. Commun.*, 2018, 9.

58 K. K. Ray, H. D. Lee, M. A. Gutierrez, F. J. Chang and A. V. Tivanski, *Anal. Chem.*, 2019, **91**, 7621–7630.

59 H. S. Morris, A. D. Estillore, O. Laskina, V. H. Grassian and A. V. Tivanski, *Anal. Chem.*, 2016, **88**, 3647–3654.

60 M. Kuwata and S. T. Martin, *Proc. Natl. Acad. Sci. U. S. A.*, 2012, **109**, 17354–17359.

61 Y. Li and M. Shiraiwa, *Atmos. Chem. Phys.*, 2019, **19**, 5959–5971.

62 Y. C. Song, A. E. Haddrell, B. R. Bzdek, J. P. Reid, T. Bannan, D. O. Topping, C. Percival and C. Cai, *J. Phys. Chem. A*, 2016, **120**, 8123–8137.

63 J. H. Slade, A. P. Ault, A. T. Bui, J. C. Ditto, Z. Lei, A. L. Bondy, N. E. Olson, R. D. Cook, S. J. Desrochers, R. M. Harvey, M. H. Erickson, H. W. Wallace, S. L. Alvarez, J. H. Flynn, B. E. Boor, G. A. Petrucci, D. R. Gentner, R. J. Griffin and P. B. Shepson, *Environ. Sci. Technol.*, 2019, **53**, 4977–4987.

64 H. S. Morris, V. H. Grassian and A. V. Tivanski, *Chem. Sci.*, 2015, **6**, 3242–3247.

65 H. D. Lee, A. D. Estillore, H. S. Morris, K. K. Ray, A. Alejandro, V. H. Grassian and A. V Tivanski, *J. Phys. Chem. A*, 2017, **121**, acs.jpca.7b04041.

66 J. D. Berry, M. J. Neeson, R. R. Dagastine, D. Y. C. Chan and R. F. Tabor, *J. Colloid Interface Sci.*, 2015, 454, 226–237.

67 A. Schwier, D. Mitroo and V. F. McNeill, *Atmos. Environ.*, 2012, **54**, 490–495.

68 A. Dazzi, F. Glotin and R. Carminati, *J. Appl. Phys.*, , DOI:10.1063/1.3429214.

69 A. Dazzi and C. B. Prater, *Chem. Rev.*, 2017, **117**, 5146–5173.

70 V. W. Or, A. D. Estillore, A. V. Tivanski and V. H. Grassian, *Analyst*, 2018, **143**, 2765–2774.

71 L. Dalstein, E. Potapova and E. Tyrode, *Phys. Chem. Chem. Phys.*, 2017, **19**, 10343–10349.

72 M. Sulpizi, M. P. Gaigeot and M. Sprik, *J. Chem. Theory Comput.*, 2012, **8**, 1037–1047.

73 D. H. Lee and R. A. Condrate, *J. Mater. Sci.*, 1999, **34**, 139–146.

74 C. J. Cros, G. C. Morrison, J. A. Siegel and R. L. Corsi, *Indoor Air*, 2012, **22**, 43–53.

75 S. Ghorai, B. Wang, A. Tivanski and A. Laskin, *Environ. Sci. Technol.*, 2014, **48**, 2234–2241.

76 C. Kaltsonoudis, E. Kostenidou, E. Louvaris, M. Psichoudaki, E. Tsiligiannis, K. Florou, A. Liangou and S. N. Pandis, *Atmos. Chem. Phys.*, 2017, **17**, 7143–7155.

77 L. Y. He, Y. Lin, X. F. Huang, S. Guo, L. Xue, Q. Su, M. Hu, S. J. Luan and Y. H. Zhang, *Atmos. Chem. Phys.*, 2010, **10**, 11535–11543.

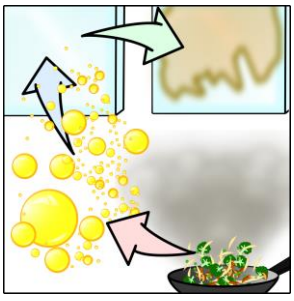

Table of contents